

# Biophysical Simulation Reveals the Mechanics of the Avian Lumbar Sacral Organ

An Mo<sup>1</sup>, Viktoriia Kamska<sup>1</sup>, Fernanda Bribiesca-Contreras<sup>1</sup>, Janet Hauptmann<sup>1,3</sup>, Monica Daley<sup>2</sup>, Alexander Badri-Spröwitz<sup>1,4</sup>

<sup>1</sup>Dynamic Locomotion Group, Max Planck Institute for Intelligent Systems, Stuttgart, Germany

<sup>2</sup>Department of Ecology and Evolutionary Biology, University of California, Irvine, USA

<sup>3</sup>Harz University for Applied Sciences, Wernigerode, Germany

<sup>4</sup>Department of Mechanical Engineering, KU Leuven, Leuven, Belgium

**Keywords:** lumbar sacral organ, intraspinal mechanosensing, physical model, biophysical simulation, spinal cord, avian locomotion

The lumbar sacral organ (LSO) is a lumbar sacral spinal canal morphology that is universally and uniquely found in birds. Recent studies suggested an intraspinal mechanosensor function that relies on the compliant motion of soft tissue in the spinal cord fluid. It has not yet been possible to observe LSO soft tissue motion *in vivo* due to limitations of imaging technologies. As an alternative approach, we developed an artificial biophysical model of the LSO, and characterized the dynamic responses of this model when entrained by external motion. The parametric model incorporates morphological and material properties of the LSO. We varied the model's parameters to study the influence of individual features on the system response. We characterized the system in a locomotion simulator, producing vertical oscillations similar to the trunk motions. We show how morphological and material properties effectively shape the system's oscillation characteristics. We conclude that external oscillations could entrain the soft tissue of the intraspinal lumbar sacral organ during locomotion, consistent with recently proposed sensing mechanisms.

## 1 Introduction

Birds are exceptional bipedal runners capable of robust running over unexpected disturbance [1]. Robust locomotion requires a sense that informs the central nervous system about the environment and the system's internal state. Such sensing is essential to coordinate limbs [2, 3], balance [4], manipulate the environment [5], for entrainments [6–9], and protect from excessive loading or untimely muscle stretching [10]. Rapid sensing and response is crucial, especially during fast locomotion. When stance phases are brief, a sensorimotor delay [11] will cause a temporal blind spot in the control loop, potentially leading to detrimental falls. Interestingly, birds generally have long necks, contributing to increased sensorimotor delays from higher brain centers, as well as from the balance-sensing vestibular system [12]. The immediate physical response of the musculoskeletal [13] system alone cannot fully explain birds' agility.

Birds' outstanding locomotion abilities might be supported by an unexplored and uniquely avian intraspinal mechanosensor: the lumbar sacral organ (LSO, Figure 1) [14]. It has been suggested that the LSO could act as a second vestibular-like sensing organ, independent of the head's orientation [14]. The LSO is located at the lower spine, right next to the sciatic nerves that communicate motor commands for locomotion [15]. The short distance between intraspinal mechanosensors and spinal motor-control units could minimize sensorimotor delays, and effectively reduce response times [16].

The LSO is a collection of unique anatomical features (Figure 2A). A glycogen body is dorsally wedged between both spinal cord hemispheres, spanning over three segments [16]. At the LSO's centre, the glycogen body ventrally reaches the central canal [17, 18]. Accessory lobes ("Hofmann nuclei" or "major marginal nuclei", [19]) are found pairwise, segmentally, and laterally to the lateral side of the spinal cord. Potentially, they contain mechanoreceptors [14, 20–25]. Hofmann nuclei processes project into ipsilateral and contralateral hemispheres [19, 26]. The spinal cord is supported

ventrally by a complex dentate ligament network, comprised of lateral longitudinal, ventral longitudinal, and transverse ligaments [16]. The vertebrae in the LSO region are fused with fusion zones formed as transverse semi-circular grooves (“semi-circular canals” [22]). Between the LSO soft tissue (spinal cord, glycogen body, dentate ligament network, accessory lobes) and the spinal canal walls exists a significant fluid space with a prominent dip ventral to the LSO central region [16].

Since its first discovery in 1811 [27], the exact function of the LSO remains an enigma. Early research suggested metabolic energy supply and myelin synthesis as potential functions for the glycogen body and accessory lobes [17, 28, 29]. Schroeder, Murray and Eide [19, 20] were the first to propose a mechanoreceptive function. They had found mechanoreceptor-like tissue in accessory lobes and therefore theorized that dentate ligament strain is transmitted to and sensed by the adjacent accessory lobes. Later, Necker proposed that semicircular grooves and spinal fluid are integral parts of the sensor organ’s function. He hypothesized that lumbosacral organ spinal fluid flow could excite mechanoreceptive accessory lobes [14, 30, 31]. Besides, he was the first to point to morphological similarities between the lumbosacral organ and the vestibular system [14]. Otherwise, possible mechanical functions of the LSO are largely unexplored. While conclusive evidence for the LSO sensing function is still missing, intraspinal mechanosensing has been found in a few animals; lampreys [32, 33], zebrafish [34, 35], and potentially in reptiles [36]. Despite the difference between these animals and birds, the similar location of their intraspinal mechanosensors is intriguing [25, 32, 35, 37], and suggests a homologous connection.

Based on our own observation of morphologies and material properties [16], we hypothesize a locomotion state sensing function of the LSO (Figure 1). We suspect that the viscoelastic properties of the spinal cord and ligaments allow these structures to physically deflect and oscillate within the enlarged fluid space [16]. During locomotion, the trunk oscillation, such as pitching, will entrain the spinal cord oscillation. The resulting soft tissue motion could resemble a mass-spring-damper system; the dense glycogen body as the mass, the elasticity of the spinal cord and the dentate ligament network as the spring, and the spinal fluid as the damper. The relative motion between the spinal cord and the spinal canal would stretch the mechanoreceptors contained in the accessory lobes, then accelerations and postural changes could be measured, leading to a fast state feedback of locomotion.

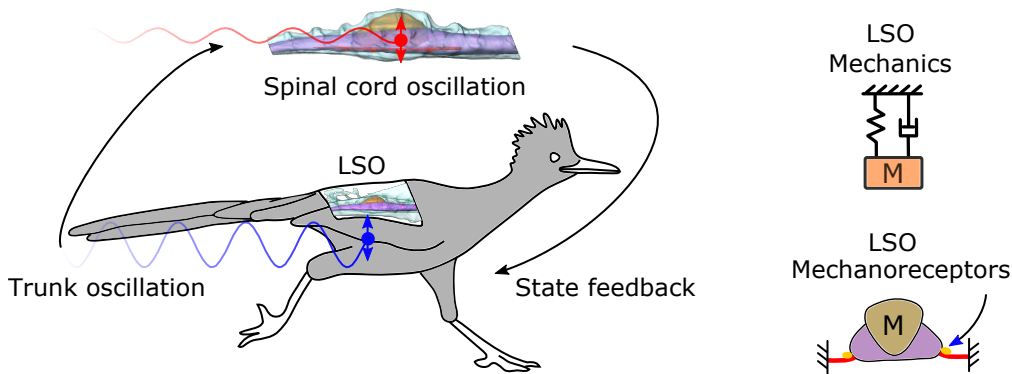


**Figure 1:** The LSO located at the lower spine of birds is hypothesized as an accelerometer. During locomotion such as running, the trunk oscillation will entrain the spine cord like a mass-spring-damper system. The morphology of LSO tunes the mass-spring-damper behavior. The entrained LSO stimulates the mechanoreceptors to provide fast state feedback of locomotion.

In this work, we focus on the mass-spring-damper properties of the LSO. Since birds feature the highest number of locomotion modes within species; they swim, dive, walk, and fly; their habitats and locomotion modalities may shape the LSO response through mass-spring-damper property variation. Structures like the glycogen body with densities higher than the spinal fluid will tend to sink, exerting forces on the dentate ligament network. The glycogen body are subject to growth [38], allowing for lifelong tuning and adaptation. The microfluidic environment of the spinal canal implies an effective flow resistance (Hagen–Poiseuille equation) to dampen high-frequency oscillation, similar to a mechanical low-pass filter. Neural tissue is fragile, with a reported maximum strain up to 7% for uni-axial fibre strain [39]. Likely, the combined structure of ligaments, spinal fluid, and glycogen body protects the spinal cord from excessive strain.

While the spinal soft tissue entrainment is likely, observing such entrainment within a running bird is a grand challenge. In birds, the spinal cord is well protected within the dense, fused bone structure. Imaging the soft tissue motion in vivo has failed so far. As an alternative approach, we developed a parametric, biophysical lumbosacral organ model, which we based on previously reported data [16]. In sum, we suggest three hypotheses related to the mass-spring-damper properties of the LSO. 1) The glycogen body tunes the LSO measurement range. 2) The narrow spinal canal dampens soft tissue oscillation. 3) The fine structure of the spinal canal diversifies the LSO response.

## 2 Materials and Methods

First, We developed a configurable biophysical model of the lumbosacral organ in birds (Figure 2). We parameterized the biophysical model’s morphology and varied its material properties to investigate the individual influence of each part and its associated hypothesis (Table 2). Then, the biophysical models were tested on a custom-built locomotion simulator (Figure 3), which emulates vertical locomotion patterns of running birds. Lastly, the biophysical model’s response to external accelerations was recorded and characterized (Figure 4).

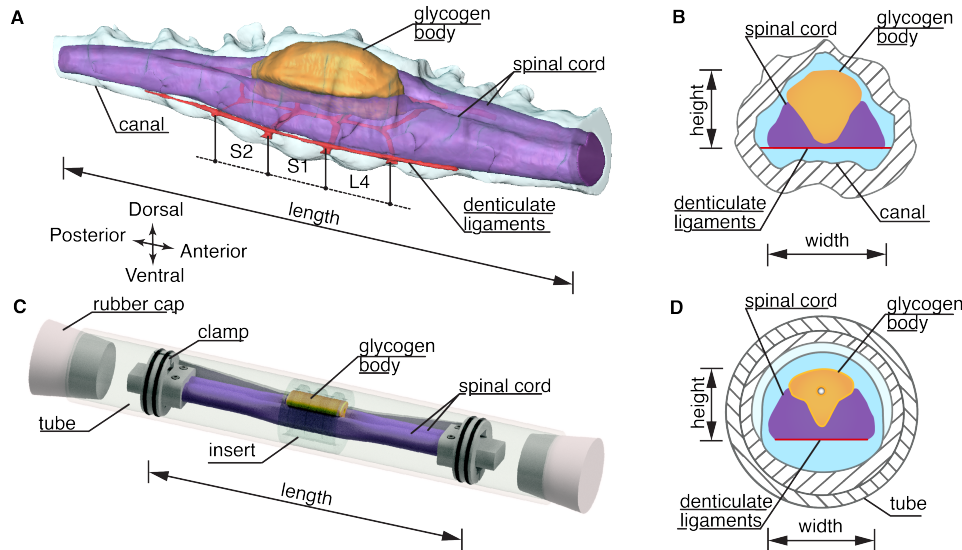


**Figure 2:** Lumbosacral soft tissue in the spinal canal, and its biophysical model developed here to simulate soft tissue motion. (A) Perspective view of the lumbosacral region of a common quail [16]. Shown are spinal cord (purple), glycogen body (orange), and dentate ligament network (red). (B) Transverse section through the vertebral column at vertebra fusion S1 and L4. (C) Biophysical model with spinal cord, glycogen body and semi-circular grooves mounted as a water-filled glass tube. In this configuration, the modelled spinal cord is clamped at its both ends. Transverse semi-circular grooves are cut into the insert as indentations. (D) Cross-cut view of the biophysical model at the position of a semi-circular groove.

### 2.1 Biophysical model

We aimed at these goals to implement and test the biophysical model of birds’ LSO: 1. Develop a simplified, parametric model for physical testing, with a low, appropriate number of design parameters. In contrast, a one-to-one replicated LSO geometry would lead to a large parameter number, which is infeasible for physical testing. 2. Select model parameters according to their relevance for the LSO’s physical functionality according to our hypotheses. 3. Create an LSO model of appropriate size for fabrication and instrumentation. 4. The ratio of volumes, material densities, and soft material stiffness approximates to data from the literature.

To replicate the geometry, we simplified and linearly scaled up the three-dimensional common quail model (*Coturnix coturnix*) made available by Kamska et al. [16]. Its main components were simplified as in the biophysical model: an spinal cord, a dentate ligament network, a glycogen body, the surrounding spinal fluid, the spinal canal morphology between spine segments L4 to S2 (Figure 2). We linearly scaled up the LSO soft parts, leading to model parameters documented in Table 1. The length of the biophysical model is 140 mm between proximal and distal anchor points (Figure 2C), which is roughly the size of the lumbosacral region of an emu [40]. We kept the volume ratio constant for the spinal cord, the glycogen body, and the spinal fluid (Table 1). We implemented model morphologies mimicking dorsal grooves and a ventral dip found in birds; both features were volume scaled.

To approximate the material properties, we fabricated the biophysical model with soft robotics techniques. The spinal cord and the glycogen body were moulded from silicone rubber, with dentate ligament network made from fabric attached. The glycogen body density is adjustable. A custom clamp holds the spinal soft tissue in a water-filled glass tube, simulating the fluid environment. A configurable insert existed in some biophysical models to implement the spinal canal morphologies. Detail fabrication steps are provided in the supplementary section S1. In sum, we prepared seven configurations of the biophysical model as shown in Table 2.

The resulting biophysical model allows for characterizing its compliant parts responding to external motions while interacting with the surrounding fluid and complex canal morphologies.

**Table 1:** Biophysical model design parameters. Volume percentages of the biophysical model are in reference to the quail model [16], for the sum of volumes at L4-S2 region.

Unit	Parameter	Reference	Design
Length [mm]	Width, $w$	3.5	21
	Length, $l$	20	140
	Height, $h$	5.0	30
Volume [mm <sup>3</sup> ]	Spinal cord, $V_{\text{SpC}}$	25 (36%)	4761 (35%)
	Spinal fluid, $V_{\text{SpF}}$	31 (45%)	6323 (47%)
	Glycogen body, $V_{\text{GB}}$	13 (19%)	2487 (18%)
Density [g/cm <sup>3</sup> ]	Spinal cord, $\rho_{\text{SpC}}$	1.0	1.0
	Spinal fluid, $\rho_{\text{SpF}}$	1.0	1.0
	Glycogen body, $\rho_{\text{GB}}$	1.4 – 1.5	1.0, 1.5, 2.0

**Table 2:** Biophysical model schematic overview. Cross-section views are made at the model centre. Blue areas represent fluid space; contours indicate canal shapes. Triangles with varying background colour/patterns represent spinal cord tissue with varying glycogen body density  $\rho_{\text{GB}}$  from 1.0 g/cm<sup>3</sup> to 2.0 g/cm<sup>3</sup>. The canal diameter indicates the inner  $\varnothing_{\text{canal}}$ . Semi-circular grooves are located on the dorsal canal inside; dips are ventral to the spinal cord. Dips and semi-circular grooves are tested in models with narrow canals only (model 4-7). All models feature a fibre-reinforced spinal cord (short horizontal red line).

Model number	1	2	3	4	5	6	7
GB density [g/cm <sup>3</sup> ]	1.0	1.5	2.0	1.5	1.5	1.5	1.5
Canal diameter [mm]	51	51	51	24	24	24	24
Canal morphology	large	large	large	grooves+dip	dip	grooves	narrow

## 2.2 Locomotion simulation

We developed a locomotion simulator to produce the up-down motion of the bird’s trunk during running (Figure 3). The locomotion simulator generates vertical motions in a controlled manner and records the biophysical model’s compliant response. A stepper motor① (103H7823-1740, *Sanyo Denki*) drives a ball screw② (KUHC1205-340-100, *MISUMI*) mounted to a frame made of 20 mm plywood③, moving a motion platform④ vertically. The 3D-printed (PLA) motion platform holds the biophysical model⑥, an LCD screen⑧ (model 1602) and a video camera⑤ (Hero 5 Black, *GoPro*). The camera and the biophysical model move together. Hence, the camera observes the model’s compliant response within the local coordinate system. A rotary encoder⑦ (AS5045, *AMS*) counts spindle rotations, and the slider displacement is the product of spindle rotation and pitch.

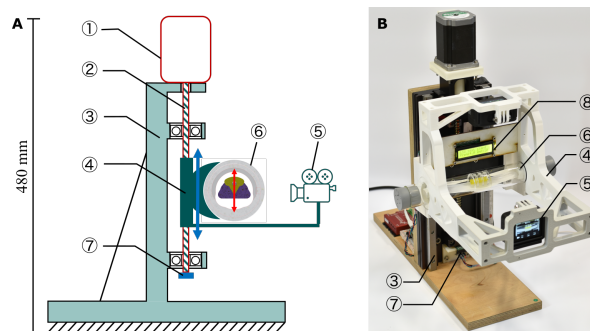


**Figure 3:** The locomotion simulator, schematic (A) and photo (B). The biophysical model⑥ is mounted to the platform④ of a linear drive③. A stepper motor① moves the slider vertically (blue) with a spindle②. An encoder⑦ records the spindle position. A camera⑤ mounted on the moving platform④ measures the biophysical model’s response (red). Video and encoder data are synchronized visually by observing the LCD screen⑧.

The locomotion simulated is instrumented. A motor driver (G201X, *geckodrive*) drives the stepper motor. A micro-controller (Teensy 4.0, *PJRC*) controls the stepper motor driver and an LCD screen. The LCD shows the setup’s status. Encoder data was sampled by a single board computer (Raspberry Pi, v.4B), with 10  $\mu\text{m}$  resolution at 1 kHz update frequency. Biophysical model movement was camera-recorded at a sampling frequency of 240 Hz. Both data lines were synchronized by a programmed LCD backlight flash. The locomotion simulator produces oscillations up to a maximum frequency of 4.5 Hz at an amplitude of  $\pm 5$  mm.

We found only a few off-the-shelf motion simulators capable of highly dynamic motion (3 Hz to 5 Hz), all of which

were expensive. With this project, we are open-sourcing<sup>1</sup> our locomotion simulator design and control for barrier-free research; which is capable, easy to replicate, and comparably low-cost.

Testing protocols were identical for all models. Glass tubes were mounted to the locomotion simulator and vertically driven to oscillate with an amplitude of  $\pm 5$  mm. We stopped the motor after 5 s. The resulting damped model motion was recorded for another 3 s. Each model was driven at four ‘drive’ frequencies: 3.0, 3.5, 4.0 and 4.5 Hz. Trials were repeated eight times, resulting in a total of 224 trials; 4 drive frequencies with 8 repetitions and 7 models.

We extracted the biophysical model’s movement from the recorded videos with the Tracker software [41]. An example trial is shown in Figure 4. We divide the experiment’s time series into three phases:

1. Entrainment phase with settling time  $\tau$ ;
2. Steady phase with peak-to-peak amplitude  $A$ , phase shift  $\phi$ ;
3. Damping phase with decay rate  $\zeta$ , damped oscillation frequency  $f_d$ .

The definitions of the measured parameters in each phase are documented in the supplementary section S2.

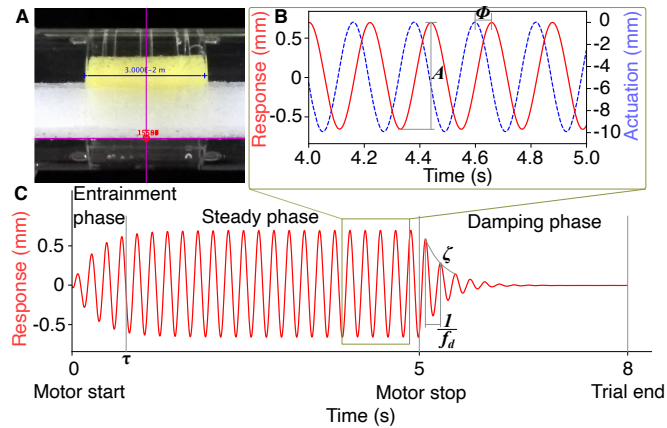


**Figure 4:** Typical model response to external motion. The data shown is extracted from trial 1, model-2, at 4.5 Hz external oscillation frequency. Each experiment shows three phases; (1) The entrainment phase, with a settling time  $\tau$  spanning from start until the model reaches 90% of the steady state amplitude. (2) In the steady phase we measure the model’s peak-to-peak amplitude  $A$ , and the phase shift  $\phi$  between the external actuation and the model’s response. (3) The damping phase starts when the motor is switched off (5 s). We calculate the model’s decay rate  $\zeta$  and the damped oscillation frequency  $f_d$ .

### 2.3 Functional parameter hypotheses

We tested three hypotheses with seven biophysical models (Table 3):

**Table 3:** Hypotheses and the corresponding control variables for model-1 to 7.

Hypothesis	Model #	Controlled variable
1	1 - 3	Density
2	2, 7	Canal size
3	4 - 7	Canal morphology

1) **The glycogen body tunes the LSO measurement range.** The glycogen body is unique in birds and unexplained. Since its density is notably higher than the surrounding spinal fluid and the spinal cord, we expect the glycogen body presents an effectively larger mass leading to higher soft tissue oscillation caused by external movements, compared to a neutrally buoyant glycogen body. We compare amplitude response and settling time of three glycogen body densities: 1.0, 1.5, and 2.0 g/cm<sup>3</sup>, and expect high glycogen body density associates with high amplitude.

2) **The narrow spinal canal dampens soft tissue oscillation.** The fluid space that allows for spinal cord oscillation is relatively small. Flow resistance increases in the proximity of walls according to the Hagen–Poiseuille equation. Hence, we expect that a narrow spinal canal increases flow resistance compared to a wide one, leading to reduced soft tissue oscillations. We investigate the effect of large and narrow canal size on the model’s response amplitude and decay rate.

3) **The spinal canal fine structure diversifies the LSO response.** Previous observations [16, 24, 42] hint the distinct spinal canal morphologies of different birds may be associated with habitats and locomotion modalities. We

<sup>1</sup>[www.github.com/moanan/1\\_dof\\_motion\\_simulator](http://www.github.com/moanan/1_dof_motion_simulator)

expect the dorsal grooves and the ventral dip [16] both have an effect on spinal fluid flow and soft tissue oscillations. To test this, we map the combinations of the dorsal grooves and the ventral dip, and study the models' response amplitude and decay rate.

### 3 Results

Table 4 shows all results obtained, ordered by model and drive frequency, symbols are identical to Table 2.

**Table 4:** Results for all models depending on drive frequency, showing settling time during entrainment phase, peak-to-peak amplitude, phase shift between drive signal and model oscillation, damped oscillation frequency and decay rate during damping phase. Values are mean values  $\pm$  standard error (SE). SEs are not shown if smaller than the rounding digit.

Model	Freq. [Hz]	Settling time $\tau$ [s]	Amp. $A$ [mm]	Phase shift $\phi$ [deg]	Damped freq. $f_d$ [Hz]	Decay rate $\zeta$ [/]
1 	3.0	$0.55 \pm 0.07$	0.11	$25 \pm 1$	4.8	$0.77 \pm 0.03$
	3.5	0.39	0.25	$28 \pm 1$	4.8	$0.69 \pm 0.02$
	4.0	$0.37 \pm 0.02$	0.62	$49 \pm 1$	4.7	0.79
	4.5	0.67	1.06	$106 \pm 1$	4.7	0.83
2 	3.0	$0.63 \pm 0.05$	0.13	$20 \pm 1$	4.8	$0.52 \pm 0.02$
	3.5	0.38	0.28	$25 \pm 1$	4.8	$0.59 \pm 0.01$
	4.0	0.36	0.66	$40 \pm 1$	4.7	$0.67 \pm 0.01$
	4.5	$0.78 \pm 0.01$	1.33	$92 \pm 1$	4.7	0.73
3 	3.0	$0.47 \pm 0.04$	0.19	$21 \pm 1$	4.5	$0.58 \pm 0.02$
	3.5	0.39	0.44	$24 \pm 1$	4.4	$0.66 \pm 0.01$
	4.0	0.61	1.03	$62 \pm 1$	4.4	0.72
	4.5	0.56	1.32	$120 \pm 1$	4.4	$0.74 \pm 0.01$
4 	3.0	0.48	0.25	$46 \pm 1$	3.7	$0.82 \pm 0.02$
	3.5	$0.72 \pm 0.02$	0.57	$80 \pm 1$	3.6	$0.87 \pm 0.01$
	4.0	0.52	0.66	$130 \pm 1$	3.6	$0.87 \pm 0.01$
	4.5	0.36	0.56	$154 \pm 1$	3.6	$0.87 \pm 0.01$
5 	3.0	$0.78 \pm 0.16$	0.06	$152 \pm 1$	$4.3 \pm 0.3$	$1.28 \pm 0.15$
	3.5	0.45	0.11	$123 \pm 1$	$4.5 \pm 0.1$	$1.53 \pm 0.16$
	4.0	0.40	0.19	$127 \pm 1$	$4.3 \pm 0.2$	$1.50 \pm 0.09$
	4.5	$0.42 \pm 0.02$	0.28	$147 \pm 1$	$4.4 \pm 0.1$	$1.42 \pm 0.14$
6 	3.0	0.48	0.25	$56 \pm 1$	3.5	$0.88 \pm 0.01$
	3.5	$0.70 \pm 0.02$	0.5	$103 \pm 1$	3.5	$0.92 \pm 0.01$
	4.0	0.40	0.5	$138 \pm 1$	3.5	$0.93 \pm 0.02$
	4.5	0.37	0.48	$155 \pm 1$	3.5	$0.89 \pm 0.02$
7 	3.0	$0.88 \pm 0.22$	0.07	$152 \pm 1$	$4.4 \pm 0.2$	$0.88 \pm 0.11$
	3.5	$0.48 \pm 0.04$	0.12	$127 \pm 1$	$5.0 \pm 0.2$	$1.24 \pm 0.18$
	4.0	$0.42 \pm 0.02$	0.19	$137 \pm 1$	$4.6 \pm 0.2$	$1.25 \pm 0.21$
	4.5	0.37	0.26	$154 \pm 1$	$4.5 \pm 0.2$	$1.02 \pm 0.13$

#### 3.1 Entrainment

All models showed an entrainment response similar to Figure 4. Within 1s models transitioned into steady-state oscillations. We observed steady-state peak-to-peak amplitude up to 1.3mm.

We observed a distinct frequency peak for each model processed with spectrum analysis. The damped oscillation frequency measured from damping phase was independent of the drive frequency for the same model, but differed between models (Table 4). Damped oscillation frequencies ranged from 3.5 Hz to 5.0 Hz. Albeit a different calculation method, damped oscillation frequencies of model 5 and 7 showed a similar dependency.

#### 3.2 Influence of glycogen body density

In general, a denser glycogen body produced a larger peak-to-peak amplitude in the steady phase. The peak-to-peak amplitude increased with increasing drive frequency (Figure 5A). The peak-to-peak amplitude significantly differed between glycogen body densities in all models at all drive frequencies ( $t$ -test;  $p$  values  $< 1e-4$ ) except for densities of

1.5 g/cm<sup>3</sup> to 2.0 g/cm<sup>3</sup> at 4.5 Hz. Model-2 with a glycogen body density of 1.5 g/cm<sup>3</sup> showed the highest peak-to-peak amplitude of 1.33 mm. Independent of glycogen body density, models took between 0.36 s to 0.78 s to entrain, and we found no clear tendency for settling time for different glycogen body densities (Figure 5B).

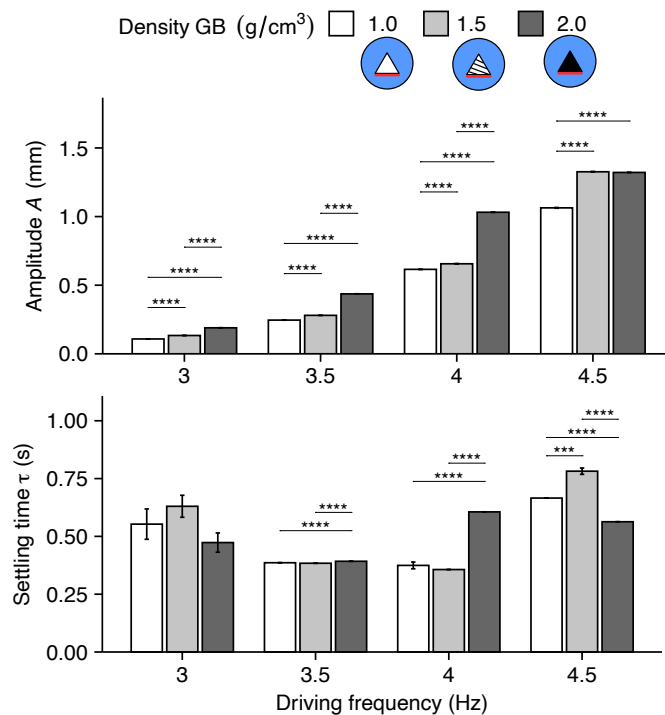


**Figure 5:** Influence of glycogen body density and drive frequency to peak-to-peak amplitude (A) and settling time (B). Values shown are for model-1, 2, and 3 with density of 1.0, 1.5, and 2.0 g/cm<sup>3</sup>, respectively. Drive frequencies tested were 3.0, 3.5, 4.0 and 4.5 Hz. Here and in all following figures, standard error shown as error bar, significant *p*-values from *t*-test pairwise comparisons as '\*\*\*\*', 0; '\*\*\*', 0-0.001; '\*\*', 0.001-0.01, '\*', 0.1-0.05. Error bars are not shown if the standard error is smaller than the measurement resolution.

### 3.3 Influence of canal size

The canal size had an effect on the soft tissue response amplitude and its decay rate (Figure 6). The larger canal of model-2 yielded a significant higher peak-to-peak amplitude of 1.33 mm at 4.5 Hz. In comparison, the narrow canal of model-7 yielded a maximum amplitude of 0.26 mm at 4.5 Hz (*t*-test; *p* values <1e-4). For both canal sizes, amplitudes increased with increasing drive frequency. A narrow canal produced damped oscillations with higher decay rate  $\zeta$  of 0.88 to 1.25, compared to a large canal with decay rates between 0.52 to 0.73. However, the difference was only significant at 3.0 Hz and 3.5 Hz (*t*-test; *p* values <0.05). The narrow canal decay rate did not increase monotonically with drive frequency as the large canal model did.

### 3.4 Influence of canal morphology

Varying canal morphologies were implemented by simulating dorsal grooves or a ventral dip (model-4 to 7, Figure 7). The peak-to-peak amplitude significantly differed between these models at all drive frequencies (*t*-test; *p* values <0.05) and it was larger in the presence of grooves+dip with values ranging from 0.25 mm to 0.66 mm, followed by dorsal grooves with values from 0.25 mm to 0.5 mm. Decay rates were lower, between 0.82 to 0.93, for models with grooves and grooves+dip. Decay rates were highest between 1.28 to 1.53 for model-5 with its ventral dip. Decay rates differed significantly only when comparing grooves+dip versus ventral dip and ventral dip versus grooves at 4.0 Hz (*t*-test; *p* values <0.05). Note that the decay rate for the narrow canal and ventral dip models showed comparatively large standard errors due to low peak-to-peak amplitude, with lower signal quality.

## 4 Discussion

We developed a reconfigurable biophysical model of the lumbosacral organ to investigate its physical response during simulated locomotion. The biophysical model includes the spinal soft tissue, the surrounding spinal fluid, and the spinal

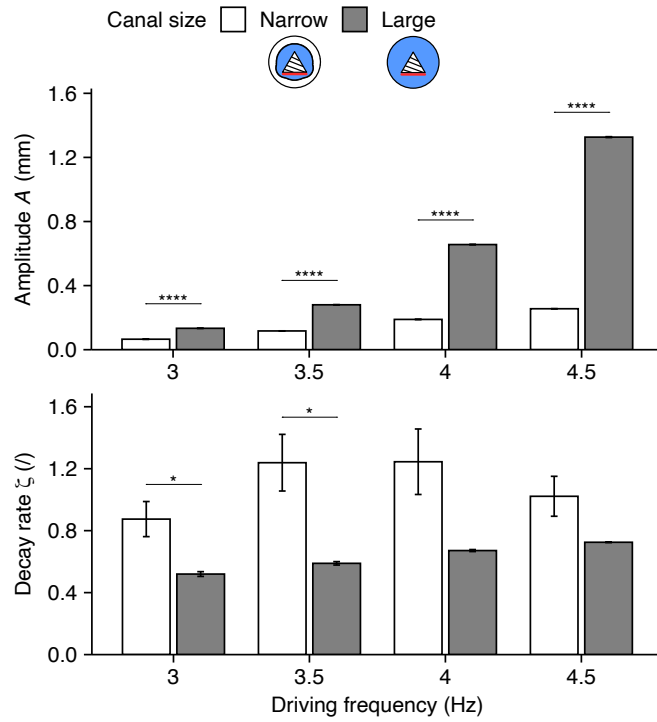


**Figure 6:** Influence of spinal canal size and drive frequency on mean values of peak-to-peak amplitude (A) and decay rate (B). Data is shown for eight trials at 3.0, 3.5, 4.0, and 4.5 Hz for model-7 with its narrow-size and model-2 with its large-size canal.

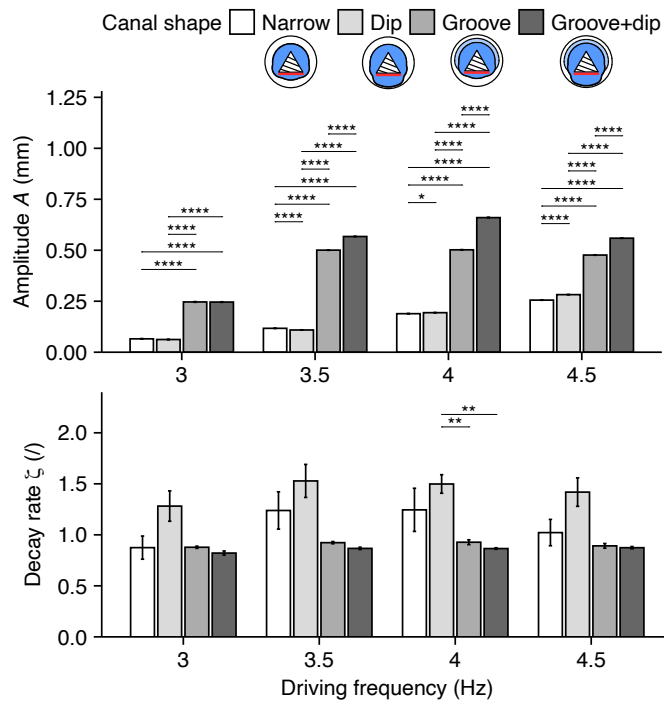


**Figure 7:** Influence of canal morphology and drive frequency on mean values of peak-to-peak amplitude(A) and decay rate (B). Data is shown for eight trials at 3.0, 3.5, 4.0, and 4.5 Hz for model-7 with a narrow canal, model-5 with a ventral dip, model-6 with a dorsal groove and model-4 with groove+dip.

canal, with a focus on replicating the key morphologies and material properties relevant to potential mechanosensing functions. The goal of this work is to produce quantitative results to understand the mechanics of the LSO, especially the influence of the glycogen body and the spinal canal. We observed typical mass-spring-damper behavior of the soft tissue oscillation, which supports the strain-based accelerometer hypothesis of the LSO [16].

The function of the LSO remains a debate in the field. The glycogen body within an enlarged spinal canal is suspicious, and can be only found in birds. Early studies assumed a “locomotor brain” function, due to the large accumulation of nerve cells nearby [43]. The glycogen body was further hypothesized to have a nutritional or secretory function [38, 44–46], or relate to myelin synthesis [17, 28]. However, these early studies failed to provide a holistic understanding of the LSO, since the specialized morphologies, such as the spinal canal and the dentate ligament network, were ignored.

Recently, new evidence has supported the mechanosensing function hypothesis of the LSO (Figure 1). The discovery of mechanoreceptive neurons within the accessory lobes laid the foundation for the potential mechanosensing function [19, 20, 22, 25, 26, 30, 31]. The enlarged spinal canal at the LSO region allows for the spinal soft tissue motion [16], which is essential for stimulating the mechanoreceptors. During locomotion, the spinal soft tissue is entrained by external acceleration, which forces the spinal fluid to circulate and the dentate ligament network to strain. Necker hypothesized that the fluid flow, guided by the spinal canal morphology, may stimulate the mechanoreceptors for a balance function [22, 24, 47, 48]. Instead of the fluid flow, Schroeder and Murray proposed that the ligament strain will transfer to the attached accessory lobes and therefore stimulate the mechanoreceptors [20]. Biological mechanoreceptors are well suited to detect the smallest strain values; they are sensitive in the angstrom range on a cellular level [49, 50]. Based on our own observations [16], the ligament strain can be up to 7.9%, which is large enough to produce consistent signals. Although none of these hypotheses have provided conclusive evidence, there were separate studies supported the LSO intraspinal sensing function. Intraspinal sensing has been identified in lamprey [32, 33] and zebrafish [34, 35], where their mechanosensors' arrangement is similar to birds' accessory lobes. Another study suggested that balance sensing exists in the bird's body. After labyrinthectomy and spinal cord transection, birds can still reflexively compensate for body rotations without the vision and vestibular sensing [51]. Here, the mechanosensing function of the LSO is a potential explanation.

The hypothesized LSO sensing mechanism can be essential for birds' exceptional locomotion agility. As agile locomotion requires fast sensing and action, the LSO potentially provides fast state feedback by minimizing the time required for detecting accelerations and sending the corresponding signals (Figure 1). On one hand, the body accelerations, as a result of contact with environments, can be transmitted to the spinal canal and the LSO through bones in the form of shock wave. The shock wave transmitted through bones [52, 53] is at least one order of magnitudes faster than the nerve conduction speed [54], allowing for fast acceleration detection. On the other hand, the close integration of LSO to the spinal cord greatly reduces the nerve conduction delays, and the output signals are likely integrated to the central pattern generator circuits for limb coordination [19, 25, 26]. Moreover, the fast state feedback is increasingly important for larger birds. An extreme example is the ancestor of birds—dinosaur, as the extended nerve fiber may prohibit in-time muscle response. Coincidentally, recent fossil records of dinosaurs have identified a lumbosacral canal enlargement similar to the birds' [55], suggesting the importance of the LSO for evolutionary success.

While the mechanosensing hypothesis has been well established [16, 20, 22, 24], several key processes remain unsolved. First, whether the spinal soft tissue can move relative to the spinal canal is still questionable. So far, we have been able to observe only a small amount of soft tissue motion in chicken [42]. Second, assuming the soft tissue can move, can truck movement entrain the spinal soft tissue motion? Further, how the morphologies and material properties shape the LSO response? In this work, we aim to understand this entrainment behavior. Third, supposing the soft tissue entrainment exists, how the neural circuits process the mechanoreceptors' signals and how the signals can be mapped to what kinds of sensing modalities is still unknown.

To answer the above questions, the main challenge is the inaccessibility of the LSO. Birds' spinal canal is densely fused, making in vivo measurement of the soft tissue movement and the mechanosensor activity almost impossible. Numerical simulation is not viable due to the complex interaction among the viscoelastic tissue, the spinal fluid, and the rigid spinal canal. Moreover, large deformation of viscoelastic materials are poorly predicted in simulation. Alternatively, we propose using biophysical simulation to study the entrainment mechanics of the LSO. Biophysical models are effective tools for testing the underlying mechanisms of biological systems [56, 57]. Benefiting from soft robotic techniques, our LSO biophysical model is parametric, modular, and based on precise anatomical data [16] (Figure 2). Testing different configurations of the biophysical model on our custom-developed locomotion simulator (Figure 3) revealed how individual morphology and material property affect the LSO response (Table 4).

The biophysical model confirmed the mobility of the soft tissue. Although the model is not a one-to-one copy of its biological reference, the underlining physics is the same. The models were carefully crafted to account for the appropriate physical forces acting on the model, such as the gravitational forces, buoyant forces, locomotion accelerations. As long as we are able to measure notable soft tissue motion, we can trust a similar soft tissue motion will exist in the biological LSO. As expected, all models have shown typical mass-spring-damper response (Figure 4). In entrainment phase, the settling time conveys how fast a model responds to external oscillation and provides an intuition of the model's temporal sensitivity. In steady phase, assuming the soft tissue displacement is in proportional to the mechanosensing signal intensity, the peak-to-peak amplitude indicates the signal strength. In damping phase, the decay rate shows how fast the LSO resets after a locomotion stop. We consider that an effective mechanosensor rapidly fades out oscillations through fluid damping and lossy tissue deformations. Here, we observed a distinct damped oscillation frequency, ranged between 3.5 Hz to 4.5 Hz, which overlaps with locomotion frequencies of running birds of 3 Hz to 5 Hz [58–60]. Note that the damped oscillation frequency is an approximation of the resonant frequency [61]. A resonating LSO will increase the oscillation amplitude, potentially increasing the sensor signal intensity. We did not perform a system identification test to determine the precise mass-spring-damper parameters, as our goal was to understand the impact of morphological variations to the LSO response, rather than systematically investigate an artificial system. In particular, we focus on the glycogen body density, the spinal canal size and morphology.

The glycogen body density showed notable influence on the soft tissue oscillation (Figure 5). We implemented the glycogen body denser than the spinal cord and the spinal fluid. In simplified mass-spring-damper systems, higher masses tend to oscillate at lower frequencies. We indeed observed a small reduction in the damped oscillation frequency between model-2 and 3 with higher glycogen body densities; from averaged 4.8 Hz to 4.4 Hz, which again confirmed the mass-spring-damper behavior. The increased glycogen body density is associated with higher peak-to-peak amplitude (Figure 5A). Since the peak-to-peak amplitude is assumed to connect with signal strength, the denser glycogen body could act as a signal amplifier. Consequently, running birds that experience higher vertical accelerations could feature a low-density glycogen body, leading to a signal intensity similar to flying or swimming birds with low-acceleration locomotion modes. As such, the glycogen body density could adjust the acceleration measurement range, i.e., amplifying small acceleration with high density, or suppressing excessive acceleration with low density. Varying glycogen body densities could have developed as a trade-off between LSO responsiveness and protection. Sudden perturbations during locomotion can lead to high accelerations, potentially damaging the spinal cord tissue. Spinal fluid and ligaments would reduce soft tissue motions through fluid buoyancy, damping, and ligament elasticity [62]. We think buoyancy could protect the best if tissue densities are similar to the surrounding fluid. Too high or low density would lead to sinking or flotation. Hence, two or more opposing motivations exist; feature a neutrally buoyant density to protect the spinal cord, and increase glycogen body density for sufficiently high peak-to-peak amplitude.

The spinal canal dimensions with submillimeter flow classifies as a micro-fluid environment, with high fluid resistance slowing the flow and dampening oscillations. The dimension of lumbosacral canal expansion has been a central question in the functional hypothesis of the LSO [14, 16, 24, 27, 63]. As expected, a narrow spinal canal led to smaller peak-to-peak amplitude and higher decay rate as a result of high damping, in contrast to a large-diameter spinal canal (Figure 6). The high damping has two main effects on the LSO sensing mechanism. First, it suppresses excessive spinal cord deflection during high acceleration events, such as strong perturbations, protecting the spinal cord tissue. Second, the resulting high decay rate enhances fast sensor reset. When locomotion stops, the damped oscillation will continue simulating the mechanosensors and generating signals. In this scenario, these signals may become noise and should be minimized as soon as possible. Therefore, the spinal canal expansion could have been optimized for the damping term of a mass-spring-damper system.

Additionally, the spinal canal enlargement features different fine structure among different birds [16, 24, 42]. From our preliminary scanning data of swan, pigeon, quail and chicken, selected to represent diverse locomotion modalities, we observed different shape of semi-circular grooves and ventral dip. We studied whether these fine structures would play an important role in the LSO response by testing the combinations of semi-circular grooves and ventral dip (Figure 7). Vertical spinal cord motions will displace fluid inside the volume-constant spinal canal; when the spinal cord moves up, the spinal fluid is pushed down. We can assume that fluid of the same volume is moved against the spinal cord motion. Lateral gaps and, possibly, semi-circular grooves will guide the flow between the spinal cord and the inner spinal canal [22, 24]. In quails [16], only small flow space is available laterally—between 0.3 mm to 0.8 mm—which we mimicked in model-4 to 7 (Table 2). Models with extra dorsal structures showed larger peak-to-peak amplitude and lower decay rates, compared to canals without (Figure 7). Hence, the laterally and dorsally extending semi-circular grooves could act as fluid reliefs or flow channels [16, 24, 48]. Model-5 featuring the ventral dip behaved somewhat unexpectedly. Albeit a larger fluid space, it caused a higher decay rate compared to the narrow-canal model-7 (Figure 7). We conclude that model-5’s ventral dip might have dampened the oscillations. Although the spinal canal we developed is highly simplified compared to our reference quail model (Figure 2), small modifications to the canal morphology has already led to considerable different responses (Figure 7). Hence, the spinal canal fine structure diversifies the LSO response, likely associated with the locomotion modality of birds. For example, we expect more pronounced semi-circular grooves and ventral dip for swimmers and divers, since the lack of visual cues and low body acceleration might require higher sensitivity. To better understand the function of spinal canal fine structure in relation to locomotion modality and LSO response, a more realistic spinal canal modelling is required.

While our three hypotheses have been validated, there are several directions for future improvement. Our locomotion simulator (Figure 3) is limited to only one degree of freedom (DoF), while real-world locomotion acceleration is in 3D space and has six DoFs. This was because suitable motion simulators capable of highly dynamic motion in six DoFs were not affordable. As a starting point, we custom-developed our own motion simulator, and open sourced the design for barrier-free research. Nevertheless, this platform was sufficient to prove the feasibility of our biophysical simulation framework. In the future, a 6-DoF motion simulator [64] will allow testing the LSO response under rolling, yawing, pitching, etc. We also expect to improve the biophysical model design by instrumentation. By adding strain or pressure sensors at the location of the mechanoreceptors (Figure 1), testing the differential mechanosensing mechanism [16] will be possible. If we can successfully map the strain or pressure signals to the body accelerations in six DoFs, we close the loop of the mechanosensing hypothesis as shown in Figure 1. More importantly, the improved and instrumented framework will permit the correlation of LSO sensitivity on specific DoF. For instance, the topology of the mechanosensors in LSO may have been optimized to predict heaving, pitching, and rolling, which are the dominant motions for most birds.

Overall, our biophysical simulation framework emphasizes the notion of understanding through creation, also known

as “What I cannot create, I do not understand.” We expect creating the “physical twins” of the LSO will be a powerful tool to improve our understanding of it.

## 5 Conclusions

We developed a simplified, modular, biophysical model of the lumbosacral organ of birds to advance our understanding of this system. Models were mounted to an instrumented setup that simulated vertical oscillations and recorded the model response. We presented results that support the central hypothesis that external motion, such as running, leads to measurable LSO spinal cord movement. The glycogen body density has a strong impact on the LSO response intensity. We found that narrow spinal canal reduces soft tissue motions through the effects of damping, effectively protecting the spinal cord. The spinal canal fine structure potentially associated with locomotion modalities of different birds. In this work, we focus on understanding the mechanics of the LSO. In the future, we expect to test the mechanosensing mechanism with a more elaborate LSO model and a 6-DoF locomotion simulator.

**Acknowledgements:** This work was supported by the China Scholarship Council (CSC) and the International Max Planck Research School for Intelligent Systems (IMPRS-IS).

**Data availability:** The biophysical model design has been uploaded as part of the supplementary material.

## References

1. Daley MA and Biewener AA. Running over rough terrain reveals limb control for intrinsic stability. *Proceedings of the National Academy of Sciences* 2006;103:15681–6.
2. Knuesel J and Ijspeert AJ. Effects of muscle dynamics and proprioceptive feedback on the kinematics and CPG activity of salamander stepping. *BMC Neuroscience* 2011;12:P158.
3. Conway BA, Hultborn H, and Kiehn O. Proprioceptive input resets central locomotor rhythm in the spinal cat. *Experimental Brain Research* 1987;68:643–56.
4. Mouel CL and Brette R. Anticipatory coadaptation of ankle stiffness and sensorimotor gain for standing balance. *PLOS Computational Biology* 2019;15. Publisher: Public Library of Science:e1007463.
5. Kuchenbecker KJ, Gewirtz J, McMahan W, et al. VerroTouch: High-Frequency Acceleration Feedback for Telerobotic Surgery. In: *Haptics: Generating and Perceiving Tangible Sensations*. Ed. by Kappers AML, Erp JBFv, Tiest WMB, and Helm FCTvd. Springer Berlin Heidelberg, 2010:189–96.
6. Goldfield EC, Kay BA, and Warren WH. Infant Bouncing: The Assembly and Tuning of Action Systems. *Child Development* 1993;64:1128.
7. Taga G. Emergence of bipedal locomotion through entrainment among the neuro-musculo-skeletal system and the environment. *Physica D: Nonlinear Phenomena* 1994;75:190–208.
8. Berthouze L and Goldfield EC. Assembly, tuning, and transfer of action systems in infants and robots. *Infant and Child Development* 2008;17:25–42.
9. Ruppert F and Badri-Spröwitz A. Learning Neuroplastic Matching of Robot Dynamics in Closed-loop CPGs. *Nature Machine Intelligence* 2022;4:652–60.
10. Haen Whitmer K. *A Mixed Course-Based Research Approach to Human Physiology*. 2021.
11. More HL and Donelan JM. Scaling of sensorimotor delays in terrestrial mammals. *Proceedings of the Royal Society B* 2018;285:20180613.
12. Urbina-Meléndez D, Jaleddini K, Daley MA, and Valero-Cuevas FJ. A physical model suggests that hip-localized balance sense in birds improves state estimation in perching: implications for bipedal robots. *Frontiers in Robotics and AI* 2018;5:38.
13. Daley MA, Voloshina A, and Biewener AA. The role of intrinsic muscle mechanics in the neuromuscular control of stable running in the guinea fowl. *The Journal of physiology* 2009;587:2693–707.
14. Necker R. Specializations in the Lumbosacral Spinal Cord of Birds: Morphological and Behavioural Evidence for a Sense of Equilibrium. *European Journal of Morphology* 1999;37:211–4.
15. Bekoff A, Stein PS, and Hamburger V. Coordinated motor output in the hindlimb of the 7-day chick embryo. *Proceedings of the National Academy of Sciences* 1975;72:1245–8.
16. Kamska V, Daley M, and Badri-Spröwitz A. 3D Anatomy of the Quail Lumbosacral Spinal Canal—Implications for Putative Mechanosensory Function. *Integrative Organismal Biology* 2020;2.

17. De Gennaro LD and Benzo CA. Ultrastructural characterization of the accessory lobes of Lachi (Hofmann's nuclei) in the nerve cord of the chick. I. Axoglial synapses. *Journal of Experimental Zoology* 1976;198:97–107.
18. Möller W and Kummer W. The blood-brain barrier of the chick glycogen body (corpus gelatinosum) and its functional implications. *Cell and Tissue Research* 2003;313:71–80.
19. Eide AL. The axonal projections of the Hofmann nuclei in the spinal cord of the late stage chicken embryo. *Anatomy and Embryology* 1996;193:543–57.
20. Schroeder DM and Murray RG. Specializations within the lumbosacral spinal cord of the pigeon. *Journal of Morphology* 1987;194:41–53.
21. Rosenberg J and Necker R. Ultrastructural characterization of the accessory lobes of Lachi in the lumbosacral spinal cord of the pigeon with special reference to intrinsic mechanoreceptors. *Journal of Comparative Neurology* 2002;447:274–85.
22. Necker R. Specializations in the lumbosacral vertebral canal and spinal cord of birds: evidence of a function as a sense organ which is involved in the control of walking. *Journal of Comparative Physiology A* 2006;192:439.
23. Yamanaka Y, Kitamura N, and Shibuya I. Chick spinal accessory lobes contain functional neurons expressing voltagegated sodium channels generating action potentials. *Biomedical Research* 2008;29:205–11.
24. Stanchak KE, French C, Perkel DJ, and Brunton BW. The Balance Hypothesis for the Avian Lumbosacral Organ and an Exploration of Its Morphological Variation. *Integrative Organismal Biology* 2020;2.
25. Stanchak KE, Miller KE, Lumsden EW, et al. Molecular markers of mechanosensation in glycinergic neurons in the avian lumbosacral spinal cord. *eNeuro* 2022.
26. Eide AL and Glover JC. Development of an Identified Spinal Commissural Interneuron Population in an Amniote: Neurons of the Avian Hofmann Nuclei. *The Journal of Neuroscience* 1996;16:5749–61.
27. Emmert A. Beobachtungen über einige anatomische Eigenheiten der Vögel. *Reil's Arch. Physiol.* 1811;10:377–92.
28. Benzo CA and De Gennaro LD. Glycogen metabolism in the developing accessory lobes of Lachi in the nerve cord of the chick: Metabolic correlations with the avian glycogen body. *Journal of Experimental Zoology* 1981;215:47–52.
29. Benzo CA and De Gennaro LD. An hypothesis of function for the avian glycogen body: A novel role for glycogen in the central nervous system. *Medical Hypotheses* 1983;10:69–76.
30. Yamanaka Y, Kitamura N, Shinohara H, Takahashi K, and Shibuya I. Analysis of GABA-induced inhibition of spontaneous firing in chick accessory lobe neurons. *Journal of Comparative Physiology A* 2012;198:229–37.
31. Yamanaka Y, Kitamura N, Shinohara H, Takahashi K, and Shibuya I. Glutamate evokes firing through activation of kainate receptors in chick accessory lobe neurons. *Journal of Comparative Physiology A* 2013;199:35–43.
32. Grillner S, Williams T, and Lagerback PA. The edge cell, a possible intraspinal mechanoreceptor. *Science* 1984;223:500–3.
33. McClellan AD and Jang W. Mechanosensory inputs to the central pattern generators for locomotion in the lamprey spinal cord: resetting, entrainment, and computer modeling. *Journal of Neurophysiology* 1993;70:2442–54.
34. Böhm UL, Prendergast A, Djenoune L, et al. CSF-contacting neurons regulate locomotion by relaying mechanical stimuli to spinal circuits. *Nature Communications* 2016;7:10866.
35. Picton LD, Bertuzzi M, Pallucchi I, et al. A spinal organ of proprioception for integrated motor action feedback. *Neuron* 2021;109:1188–1201.e7.
36. Schroeder DM. The marginal nuclei in the spinal cord of reptiles: intraspinal mechanoreceptors. *The Ohio Journal of Science* 1986;86:69–72.
37. Viana Di Prisco G, Walle'n P, and Grillner S. Synaptic effects of intraspinal stretch receptor neurons mediating movement-related feedback during locomotion. *Brain Research* 1990;530:161–6.
38. Watterson RL and Spiroff BEN. Development of the Glycogen Body of the Chick Spinal Cord. II. Effects of Unilateral and Bilateral Leg-Bud Extirpation. *Physiological Zoology* 1949;22:318–37.
39. Tamura A, Nagayama K, Matsumoto T, and Hayashi S. Variation in nerve fiber strain in brain tissue subjected to uniaxial stretch. *Stapp car crash journal* 2007;51:139–54.
40. Bausch P. Die Spezialisierungen des lumbosakralen Wirbelkanals beim Großen Emu (*Dromaius novaehollandiae*). Tech. rep. 2014.
41. Software T. Tracker Video Analysis and Modeling Tool for Physics Education.
42. Kamska V, Mo A, Pohmann R, Karakostis FA, Daley MA, and Badri-Spröwitz A. Imaging the soft tissues motion inside the canal, submitting.
43. Streeter GL. The structure of the spinal cord of the ostrich. *American Journal of Anatomy* 1904;3:1–27.

44. Terni T. Ricerche sulla cosiddetta sostanza gelatinosa (corpo glicogenico) del midollo lombo-sacrale degli uccelli... L. Niccolai, 1924.
45. De Gennaro LD. The carbohydrate composition of the glycogen body of the chick embryo as revealed by paper chromatography. *The Biological Bulletin* 1961;120:348–52.
46. Azcoitia I, Fernandez-Soriano J, and Fernandez-Ruiz B. Is the avian glycogen body a secretory organ? *Journal fur Hirnforschung* 1985;26:651–7.
47. Necker R. Head-bobbing of walking birds. *Journal of comparative physiology A* 2007;193:1177.
48. Necker R, Janßen A, and Beissenhirtz T. Behavioral evidence of the role of lumbosacral anatomical specializations in pigeons in maintaining balance during terrestrial locomotion. *Journal of Comparative Physiology A* 2000;186:409–12.
49. Hudspeth AJ. How the ear’s works work. *Nature* 1989;341. Publisher: Nature Publishing Group:397–404.
50. Barth FG. Mechanics to pre-process information for the fine tuning of mechanoreceptors. *Journal of Comparative Physiology. A, Neuroethology, Sensory, Neural, and Behavioral Physiology* 2019;205:661–86.
51. Biederman-Thorson M and Thorson J. Rotation-compensating reflexes independent of the labyrinth and the eye. *Journal of comparative physiology* 1973;83:103–22.
52. Pelker RR and Saha S. Stress wave propagation in bone. *Journal of Biomechanics* 1983;16:481–9.
53. Miller TE and Mortimer B. Control vs. constraint: understanding the mechanisms of vibration transmission during material-bound information transfer. *Frontiers in Ecology and Evolution* 2020;8:587846.
54. More HL, Hutchinson JR, Collins DF, Weber DJ, Aung SK, and Donelan JM. Scaling of sensorimotor control in terrestrial mammals. *Proceedings of the Royal Society B: Biological Sciences* 2010;277:3563–8.
55. Wedel M, Atterholt J, Dooley A, et al. Expanded neural canals in the caudal vertebrae of a specimen of *Haplocanthosaurus*. *Acad. Lett* 2021;911.
56. Panjabi MM. Cervical spine models for biomechanical research. *Spine* 1998;23:2684–99.
57. Poel R, Belosi F, Albertini F, et al. Assessing the advantages of CFR-PEEK over titanium spinal stabilization implants in proton therapy—a phantom study. *Physics in Medicine & Biology* 2020;65:245031.
58. Gatesy S and Biewener A. Bipedal locomotion: effects of speed, size and limb posture in birds and humans. *Journal of Zoology* 1991;224:127–47.
59. Smith NC, Jespers KJ, and Wilson AM. Ontogenetic scaling of locomotor kinetics and kinematics of the ostrich (*Struthio camelus*). *Journal of Experimental Biology* 2010;213:1347–55.
60. Daley MA and Birn-Jeffery A. Scaling of avian bipedal locomotion reveals independent effects of body mass and leg posture on gait. *Journal of Experimental Biology* 2018;221:jeb152538.
61. Morin D. Oscillations. In: *Waves*. 2021. Chap. 1.2:15.
62. Telano LN and Baker S. *Physiology, Cerebral Spinal Fluid*. In: Treasure Island (FL): StatPearls Publishing, 2022.
63. Necker R. The structure and development of avian lumbosacral specializations of the vertebral canal and the spinal cord with special reference to a possible function as a sense organ of equilibrium. *Anatomy and Embryology* 2005;210:59–74.
64. Pradhan NMS, Frank P, Mo A, and Badri-Spröwitz A. Upside down: affordable high-performance motion platform. arXiv preprint arXiv:2303.17974 2023.